

Unravelling Structural, Optical, and Band Alignment Properties of Mixed Pb-Sn Metal-Halide Quasi-2D Ruddlesden-Popper Perovskites

Peer-reviewed author version

Deshpande, Shatayu S.; Saykar, Nilesh G.; Mandal, Animesh; Rahane, Swati; Jadhav, Yogesh A.; Kahaly, M. Upadhyay; Nagy, G. N.; Shinde, Aparna; SURESH, Sunil & Rondiya, Sachin R. (2024) Unravelling Structural, Optical, and Band Alignment Properties of Mixed Pb-Sn Metal-Halide Quasi-2D Ruddlesden-Popper Perovskites. In: Langmuir, 40 (31) , p. 16180 -16189.

DOI: 10.1021/acs.langmuir.4c01278

Handle: <http://hdl.handle.net/1942/43658>

Unravelling Structural, Optical, and Band Alignment Properties of Mixed Pb-Sn Metal Halide Quasi-2D Ruddlesden Popper Perovskites

Shatayu S. Deshpande,^a Nilesh G. Saykar,^a Animesh Mandal,^a Swati Rahane,^b Yogesh A. Jadhav^c, M. Upadhyay Kahaly^d, G. N. Nagy^d, Aparna Shinde^e, Sunil Suresh^{f,g,h}, Sachin R. Rondiya^{*a}

^aDepartment of Materials Engineering, Indian Institute of Science, Bangalore-560012, India

^bDepartment of Physics, Savitribai Phule University, Pune- 411007, India

^cSymbiosis Center for Nanoscience and Nanotechnology (SCNN), Symbiosis International (Deemed University) (SIU), Lavale, Pune 412115, Maharashtra, India

^dELI- ALPS, ELI-HU Non-Profit Ltd., Wolfgang Sandner utca 3., Szeged 6728, Hungary

^eDepartment of Experimental Physics, Faculty of Fundamental Problems of Technology, Wrocław University of Science and Technology, Wrocław 50-370, Poland

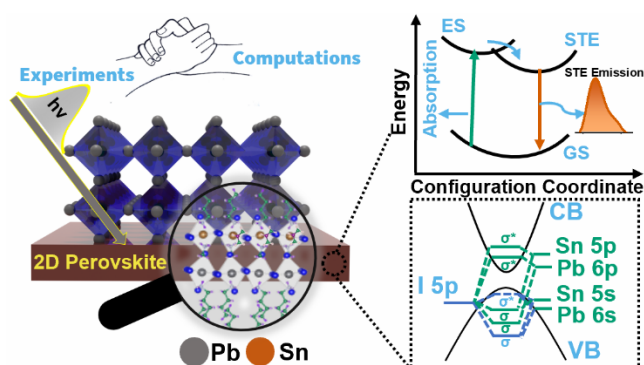
^fInstitute for Material Research (IMO), Hasselt University, Diepenbeek B-3590, Belgium

^gIMEC Division IMOMEC – Partner in Solliance, Wetenschapspark 1, Diepenbeek B-3590, Belgium

^hEnergyVille, Thor Park 8320, Genk B-3600, Belgium

Corresponding Author e-mail*: rondiya@iisc.ac.in

TOC GRAPHIC



ABSTRACT

Lead-tin (Pb–Sn) mixed halide perovskites show potential for single-junction and tandem solar cells due to their adjustable bandgaps, flexible composition, and superior environmental stability compared to three-dimensional (3D) perovskites. However, they have lower power conversion efficiencies. Understanding band alignment and charge carrier dynamics is essential for enhancing their photovoltaic performance. In this view, herein we have prepared thin films of mixed Pb-Sn based 2D Ruddlesden-Popper (RP) perovskite $\text{BA}_2\text{FA}(\text{Pb}_{1-x}\text{Sn}_x)_2\text{I}_7$ using a solution-based method. XRD study revealed the formation of orthorhombic phases for Pristine ($\text{BA}_2\text{FAPb}_2\text{I}_7$) and mixed Pb-Sn perovskite thin films. UV-Vis analysis showed that different $n=2$ and $n=3$ phases are present in the Pristine Sample. In contrast, Pb-Sn doped-based samples showed no signature of other phases with a prominent red shift in the visible spectral region. Cyclic voltammetry showed peaks for electron transfers at band edges. Additionally, electrochemical and optical bandgap matching was observed, along with decreased peak intensity due to less reactant and altered electrolyte-perovskite interface stability. DFT calculations revealed that the reduced bandgap is due to the alteration of electrostatic interactions and charge distribution within the lattice upon Sn substitution. Low-temperature PL analysis provided insights into charge carrier dynamics with Sn substitution and suggested suppressing higher n phases and self-trapped excitons/carriers in mixed Pb-Sn quasi-2D RP perovskite thin films. This study sheds light on the electron transfer phenomena between TiO_2 and SnO_2 layers by estimating band offsets from VBM and CBM, which is crucial for future applications in fabricating stable and efficient 2D Pb-Sn mixed perovskites for optoelectronic applications.

KEYWORDS

Mixed Pb-Sn perovskite, 2D Ruddlesden-Popper perovskite, temperature-dependent photoluminescence, Self-trapped excitons, lead-free perovskites.

INTRODUCTION

The last few years have witnessed rapid growth and development in hybrid halide perovskite thin films. This emergence began from 3D perovskites, as they possess remarkable electronic and optical properties¹ such as high defect tolerance^{2,3}, solution processibility^{4,5}, excellent charge transport^{6,7}, light harvesting capability^{8,9}, high absorption coefficient^{10,11}, long carrier diffusion^{12,13}. Despite these advantages, they also have inherent instability issues resulting from ion migration and moisture erosion^{1,14}. However, 2D RP Perovskite has shown exciting characteristics because of its layered structure obtained by introducing a significantly larger (than ordinary cations) A' cation called as spacer cation between inorganic octahedral slabs of BX₃¹⁴. These types of arrangements show excellent ambient stability, outstanding device performance, large exciton binding energies, and quantum and dielectric confinement effects^{15–19}. The general formula of 2DRP is (A')₂(A)_{n-1}B_nX_{3n+1} where A' is a monovalent organic spacer cation (Ex: - BA⁺ = n- butylammonium), A is monovalent organic cation (Ex: - FA⁺ = Formamidinium), B is divalent metal cation (Ex: - Pb²⁺, Sn²⁺), X is Halide anion (Ex: - I⁻) and n is the thickness of inorganic octahedral slabs²⁰.

Compared to 3D perovskites, the 2D perovskites (n = 1) possess strong dielectric and quantum confinement, preventing out-of-plane charge carrier transport. However, as the value of n increases, a significant improvement in the photophysical properties of quasi-2D perovskite (n > 1) is observed, leading to excitonic effects and opulent excitonic physics²¹. Low exciton binding energy (E_b) in 3D perovskite leads to exciton dissociation at room temperature; thus, small radiative recombination efficiency is observed. The 2DRP counterparts show improved radiative recombination because of the high exciton binding energy²². Metal Halide Perovskites (MHPs) based solar cells are categorized into three sections: lead-based, mixed lead-based, and lead-free perovskites. The lead-based perovskites have shown improved efficiency from 3.8%²³ to 26.1%²⁴. Till now, most of the research has been focused on Pb-based perovskites, but as Pb is toxic, there is a continuous urge to find an alternative of lead-free or mixed lead-based perovskite materials. Among them, Pb-Sn mixed perovskites are the only alternative with a bandgap in the desired range and performance close to lead-based perovskites. Additionally, these perovskites have shown ideality for developing single-junction devices, and the toxicity has also been reduced for Pb-Sn mixed perovskites²⁵.

Proper alignment and low energy band offset between perovskite and charge transport layers are crucial for efficient charge collection. Metal oxides such as TiO_2 and SnO_2 have great potential due to their excellent properties, like CBM alignment with perovskites with low energy offset, transparency, and high mobility, producing highly efficient and stable perovskite solar cells. For instance, meso- TiO_2 is reported to be a highly stable and efficient ETL, reaching record efficiency. However, the low electron mobility compared to SnO_2 limits its application for further improvement. Nowadays, SnO_2 has been widely used as ETL for planar perovskite solar cells. Yuhei Ogomi et al. reported for the first time the Pb-Sn mixed perovskite where they confirmed Pb-Sn mixed perovskites as a competitive light-absorbing material²⁶. Several reports have shown higher carrier diffusion lengths and lifetime for Pb-Sn mixed perovskites. A few years back, Pb-Sn mixed perovskites reported an increase in a lifetime up to $9\mu\text{s}$ ²⁷. Siyi Xian et al. reported that preparing a defect-free quasi-2D perovskite film with outstanding photoelectric properties is challenging due to unavoidable defects; they showed $\text{BA}_2\text{FAPb}_2\text{I}_7$ as a photo-responsive material. Additionally, it showed lesser trap density, higher carrier mobility, and effective light capturing. They have also reported different excitonic and defect state emissions via temperature-dependent photoluminescence spectroscopy²⁸. Yi Yang et al. revealed that Sn, possessing similar properties to Pb, exhibits smaller bandgaps, lower exciton binding energies, and higher carrier mobility²⁹.

In this work, we have demonstrated an approach for replacing Pb with Sn in a stoichiometric ratio for the material $\text{BA}_2\text{FA}(\text{Pb}_{1-x}\text{Sn}_x)_2\text{I}_7$ ($x = 0, 0.25, 0.50$). A facile solution-based synthesis approach is used, which involves one-step spin coating followed by annealing³⁰. An obvious lattice contraction is observed on the partial substitution of Pb with Sn. It was also found that the large n phases were suppressed by incorporating Sn. Temperature-dependent photoluminescence, time-resolved photoluminescence spectroscopy, and cyclic voltammetry techniques were employed to interpret the samples' charge carrier recombination kinetics, electronic band structure, and electronic band gap. It is found that lead-rich 2DRP thin films exhibit the self-trapped excitons. However, the incorporation of Sn reduced the STE emissions. The potential of the prepared $\text{BA}_2\text{FA}(\text{Pb}_{1-x}\text{Sn}_x)_2\text{I}_7$ 2DRP material is evaluated for optoelectronic applications by calculating energy band offset with ETLs.

EXPERIMENTAL METHODS, MATERIAL CHARACTERIZATION, AND COMPUTATIONAL METHODS

Materials

All the chemicals were of analytical reagent grade with high purity. n-Butylammonium Iodide (BAI, 99.9%), Formamidinium Iodide (FAI, 99.9%), Lead Iodide (PbI_2 , 99.9%), Tin Iodide (SnI_2 , 99.9%), Tetra butyl ammonium perchlorate (TBAP 99.9%) Ferrocene, Dichloromethane (DCM), 0.5 μm Al_2O_3 powder, Toluene, Titanium VI isopropoxide (TTIP) ($\text{Ti}[\text{OCH}(\text{CH}_3)_2]_4$ 99.999% purity, Sigma-Aldrich, Tin(IV) oxide, 15% in H_2O colloidal dispersion Thermo Fischer, Titania Paste (Sigma Aldrich), Dimethyl Formamide (DMF, 99.8%), Dimethyl Sulfoxide (DMSO, 99.9%), Chlorobenzene were purchased from Sigma-Aldrich and were used as received.

Synthesis of Quasi-2D perovskites

Corning glass is used as the substrate for the deposition of thin film, which was ultrasonically cleaned using distilled water, acetone, and isopropyl alcohol successively, followed by dry cleaning with nitrogen gas before transferring it into the glove box. The precursor solution was prepared in a mixed solvent of DMF and DMSO (3:2, V/V) with 0.31 M BAI, 0.16 M FAI, and 0.31 M PbI_2 and the appropriate amount of SnI_2 were used to prepare $\text{BA}_2\text{FA}(\text{Pb}_{1-x}\text{Sn}_x)_2\text{I}_7$ ($x=2$). To prevent oxidation of Sn^{2+} to Sn^{4+} , SnF_2 (10%) was added. The precursor solution was spin-coated at 4000 rpm for 30 secs on cleaned corning glass. Antisolvent chlorobenzene (300 μL) was added during the last 5 seconds of the spinning process. Lastly, the thin films were annealed at 100 $^\circ\text{C}$ for 30 mins³⁰. The whole process is carried out in the glove box. Shown in Figure S1

Structural, Optical, and Morphological Characterization

X-ray diffractogram of 2D perovskite thin films was performed on Bruker D8 advance (2.2 KW, 40 mA) with Cu K_α source radiation ($\lambda = 1.546 \text{ \AA}$) with $\theta - 2\theta$ scan mode ranging from 5 $^\circ$ to 50 $^\circ$ at 2.25 degrees/min. Optical (ultra-violet) absorption spectra were recorded using Perkin-Elmer Lambda 1050+ spectrophotometer. The steady-state PL spectra and temperature-dependent PL spectra were recorded using a Horiba Fluorolog FL3 spectrometer with a Xenon lamp as an excitation source and a PMT detector. Time-resolved PL was recorded on Horiba Jobin Yvon Fluorocube -01-NL fluorescence lifetime system under picosecond laser diode excitation with 405 nm as excitation wavelength, which includes optical pulse duration <70 ps and highly integrated picosecond PMT modules. Scanning electron micrographs were recorded using an Ultra55 Field Emission scanning electron

microscope by Karl Zeiss. Atomic Force Micrographs were recorded using the ParkNX20 instrument in Tapping mode and using HQ: NSC15/AI BS tips. High-resolution imaging was done in an aberration-corrected TEM in HR-TEM mode (FEI Titan Themis) operated at 300 kV. X-ray photoelectron spectroscopy (XPS) measurements are carried out using a PHI 5000 VERSA PROBE III ULVAC PHI instrument (Physical Electronics, USA) to investigate each element's chemical environment/state. Monochromatic Al K α radiation at 1486.6 eV is employed as the X-ray source. The base vacuum of the XPS chamber is maintained at a level above 10^{-9} torr. The peak position of C1s in the survey scan is compared with the standard value of 284.5 eV to correct for any shifts in each element's binding energy (spectral position) (C, N, O, Pb, Sn, I).

Electrochemical Characterization - Cyclic Voltammetry (CV)

Cyclic voltammetry measurements were conducted using an electrochemical workstation, specifically the Metrohm Potentiostat/Galvanostat Autolab PGSTAT 302N as per our previous protocol.^{31–34} In this setup, a commercial glassy carbon (GC) disk electrode (2-mm, CHI Instruments, USA), silver wire, and platinum wire loop serve as the working, quasi-reference, and counter electrodes. Both metal electrodes (Ag, Pt wire) undergo cleaning in dilute nitric acid to prevent surface contamination during voltammetric measurement. The GC electrode undergoes cleaning with 0.5 μm Al₂O₃ powder and subsequent rinsing with DI water. Following the cleaning process, all three electrodes are dried within a custom 5-neck electrochemical cell under vacuum and nitrogen. The measurements are conducted under positive argon pressure. A pre-dried solution containing 100 mM of TBAP in dichloromethane (DCM, 10 mL) is introduced into the electrochemical cell through a silicone septum. Controlled cyclic voltammetry (CV) is recorded in the TBAP-DCM system without loading the as-prepared nanoparticles. Subsequently, the GC electrode is loaded with 50 μL of sample dispersion toluene (1 mg mL⁻¹) and subjected to vacuum drying. A consistent scan rate of 50 mV s⁻¹ is maintained for all measurements. Finally, ferrocene is used for internal calibration, and potentials are calibrated to standard for the normal hydrogen electrode (NHE).³⁴

Computational Details

DFT calculations were conducted using the Amsterdam Molecular Suite (AMS). Double Zeta plus Polarization (DZP) basis, Spin-unrestricted calculation, with GGA PBE pseudopotential. Multiple Pb sites were required to consider the doping of Sn ions in Pb sites

and different doping concentrations. Hence, 2x2x1 supercell has been adopted for all calculations, along with 4x4x6 k points to represent irreducible Brillouin zone for obtaining band structure. We performed variable cell structure optimization (VC-relax) on undoped (x=0) structure, and further structural optimization on doped structures was carried out using the optimized undoped cell.

RESULTS AND DISCUSSION

Figure 1a shows the X-ray diffractogram of thin films of $\text{BA}_2\text{FA}(\text{Pb}_{1-x}\text{Sn}_x)_2\text{I}_7$ (x = 0, 0.25, 0.5). The characteristic peaks in the XRD spectra of Sn0 at 4.29° , 8.79° , 13.32° , and 27.05° are correspond to the crystal's planes (020), (040), (060), (0120) respectively. It reveals that Sn0 crystallizes in an orthorhombic crystal structure with space group symmetry of (Cc2m). On incorporation of Sn in $\text{BA}_2\text{FA}(\text{Pb}_{1-x}\text{Sn}_x)_2\text{I}_7$, a slight shift to the higher angle was observed in the peak position shown in Figure S2. However, peak broadening is clearly observed in Sn25 and Sn50 thin films. The crystallite size and microstrain were calculated using the Scherrer Equation; we identified a decrease in crystallite size and an increase in microstrain and Dislocation density. Additionally, the shift of peaks to higher angles suggests the presence of compressive strain. The effect of Sn addition on the surface morphology of the prepared films is investigated by FESEM, as shown in Figure 1b. The Sn0 thin films show a uniform and compact surface, whereas adding 25% Sn shows the explicit grains and rough surface may be due to the fast and uncontrolled crystallization (Figure S3 a and b). Thin films of Sn25 contain more voids and pinholes than Sn0 and Sn50. The FESEM image of the Sn50 shows a uniform and compact surface compared to that of the Sn25; however, the Sn50 possesses some grain striations. Additionally, we have performed atomic force microscopy (AFM) of Sn25 thin films to verify the surface characteristics of thin films. It has been observed that the elemental composition of the Pb and Sn in Sn0 and Sn50 are found to be consistent with the stoichiometric ratio (Figure S3 c and d). However, the Sn content in the Sn50 is found to be a little more. It may be observed due to adding the 10% excess SnF_2 . From 2D AFM images (Figure 1c), we can confirm that the small distinct grains are consistent with FESEM. In the 3D topographic AFM images (Figure 1d), we can see the rough surface and roughness calculated to be 12.37 nm.

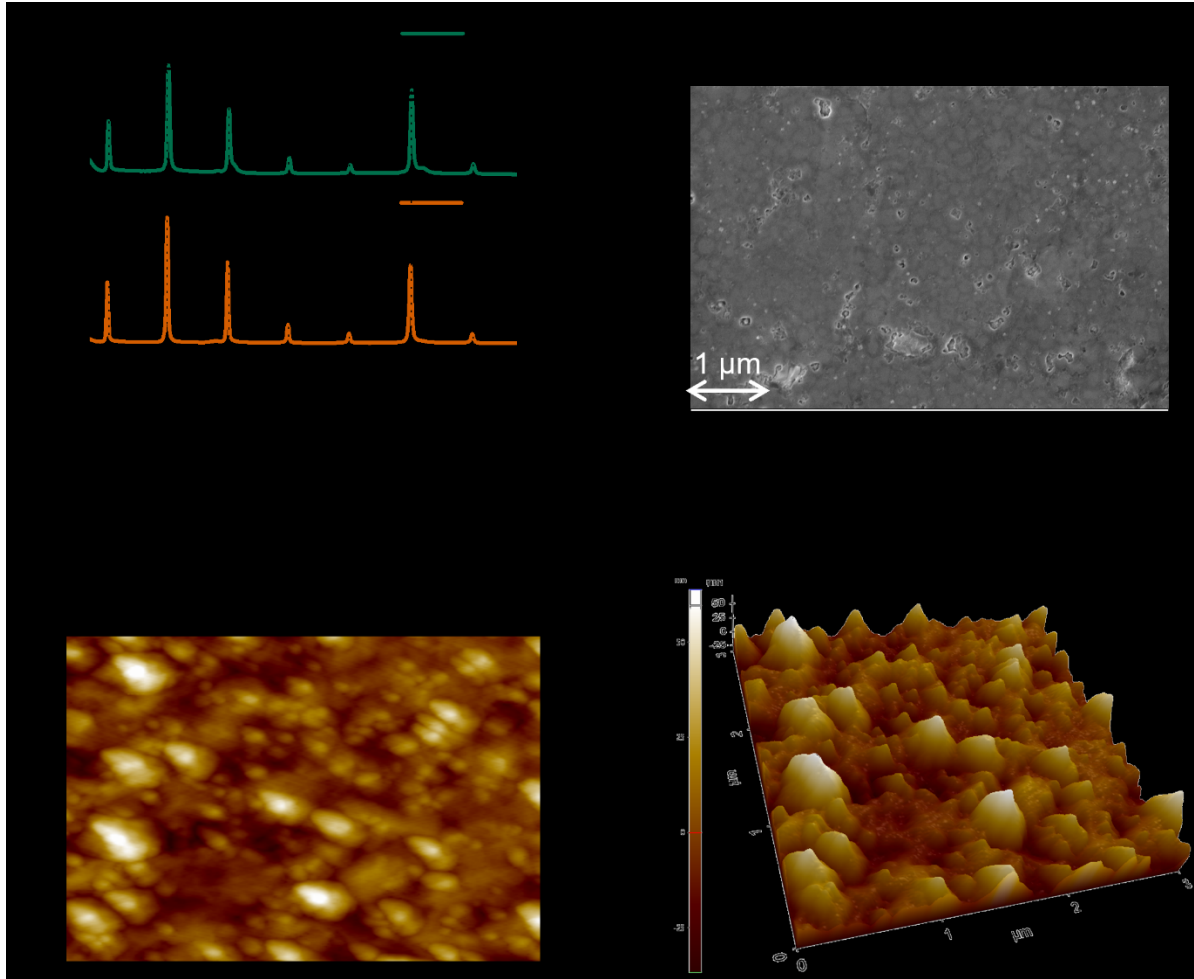


Figure 1. (a) X-ray diffraction spectra, (b) Field Emission Scanning Electron Microscopy Image of Sn50, (c) 2D Atomic force Microscopy Image of Sn50, (d) 3D Atomic force Microscopy Image of Sn50.

High-resolution TEM imaging was used to understand morphological and structural information of samples at the nanoscale level. A Low-resolution TEM image recorded at 100 nm is shown in Figure 2a. The HR-TEM images of the Sn50 (Sn-Based 2d perovskite) sample shown in Figure 2b have lattice fringes with an interplanar distance $d = 0.317$ nm, which can be assigned to the (0120) plane, and a $d = 0.68$ nm interplanar distance indicates these planes to be of (060) character, are approximately matching with the data obtained from XRD pattern. The concentric rings observed in the SAED pattern (Figure 2c) show the polycrystalline nature, and the four peaks are in agreement with the XRD analysis.

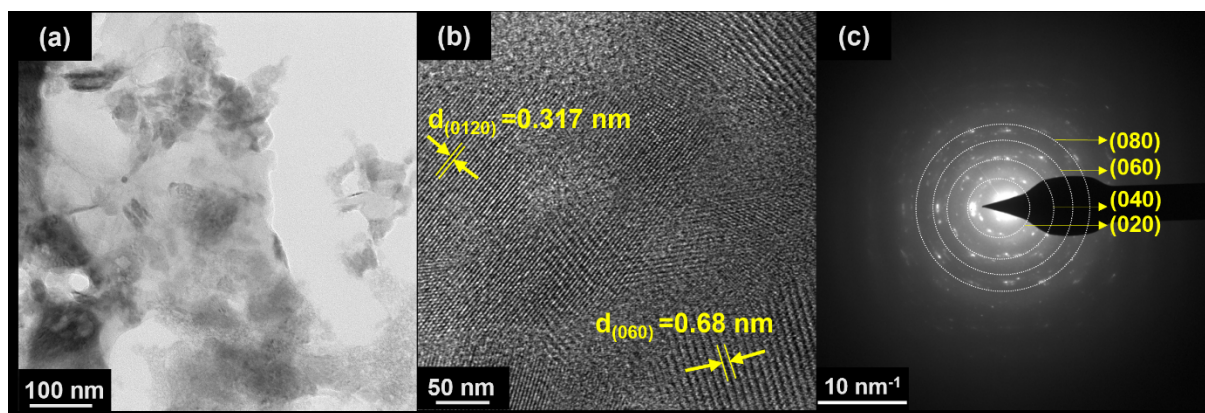


Figure 2. (a) Low magnification TEM image of Sn50 sample, (b) High-resolution TEM image, (c) Its corresponding SAED pattern with a white circle on designated (hkl) planes.

X-ray photoelectron spectroscopy (XPS) is used to study the effect of Sn doping in the quasi-2D perovskite thin films. The survey scan of XPS is shown in the supporting information in Figure S4. All the spectra are corrected to C1s before plotting. Figure 3a shows the Pb4f core level spectra of pure quasi 2D perovskite and Sn incorporation quasi 2D perovskite. The two distinct peaks corresponding to the Pb 4f_{5/2} and Pb 4f_{7/2} with binding energy (B.E.) 142.2 and 137.4 eV, respectively, are observed³⁵. Along with these dominating peaks, the deconvolution of Pb 4f spectra of Sn0 shows two small peaks at higher energies, which corresponds to metallic Pb⁰ having B.E. of 143.25 eV and 138.45 eV respectively³⁶. The appearance of metallic Pb indicates that although we take stoichiometric ratio in precursors, the excess lead is present in pure quasi 2D perovskite thin films. However, the Pb4f core level spectra of Sn25 and Sn50 in Figures 3b and c reveal that peaks related to metallic Pb⁰ have vanished, indicating that Sn doping suppresses the Pb⁰ defects in Sn-based quasi 2D perovskite thin films. Perhaps the Pb 4f_{5/2} and Pb 4f_{7/2} peaks are shifted to higher B.E., as shown in Figure 3d by 300 meV. This may be due to the contraction of the crystal lattice. Generally, in tin-based perovskites, the Sn²⁺ oxidizes to the Sn⁴⁺, causing the fast degradation of the perovskite thin films. To suppress the oxidation of Sn²⁺, most of the studies recommended the addition of SnF₂ in precursors, so accordingly, we followed the same strategy. The Figure 3d and e shows XPS core level spectra of Sn25 and Sn50 quasi 2D perovskite thin films. The Gaussian fitting of the Sn core level spectra of Sn25 shows the two intense peaks corresponding to Sn 3d_{5/2} and Sn 3d_{3/2} at BE of 486.68 and 495.23 eV (Figure). We can see that there is no signature of the Sn⁴⁺ peak as the Gaussian function fits well for Sn²⁺ only, which improves the stability of perovskite thin films. However, Sn core level spectra in Figure 3e of Sn50 shows an additional 2 peaks other than Sn²⁺ at BE 486.15 and 497.15 related to Sn⁴⁺. The appearance

of these peaks indicates that the Sn50 quasi 2D perovskite films contain more oxidized Sn^{4+} and may be form unstable films.

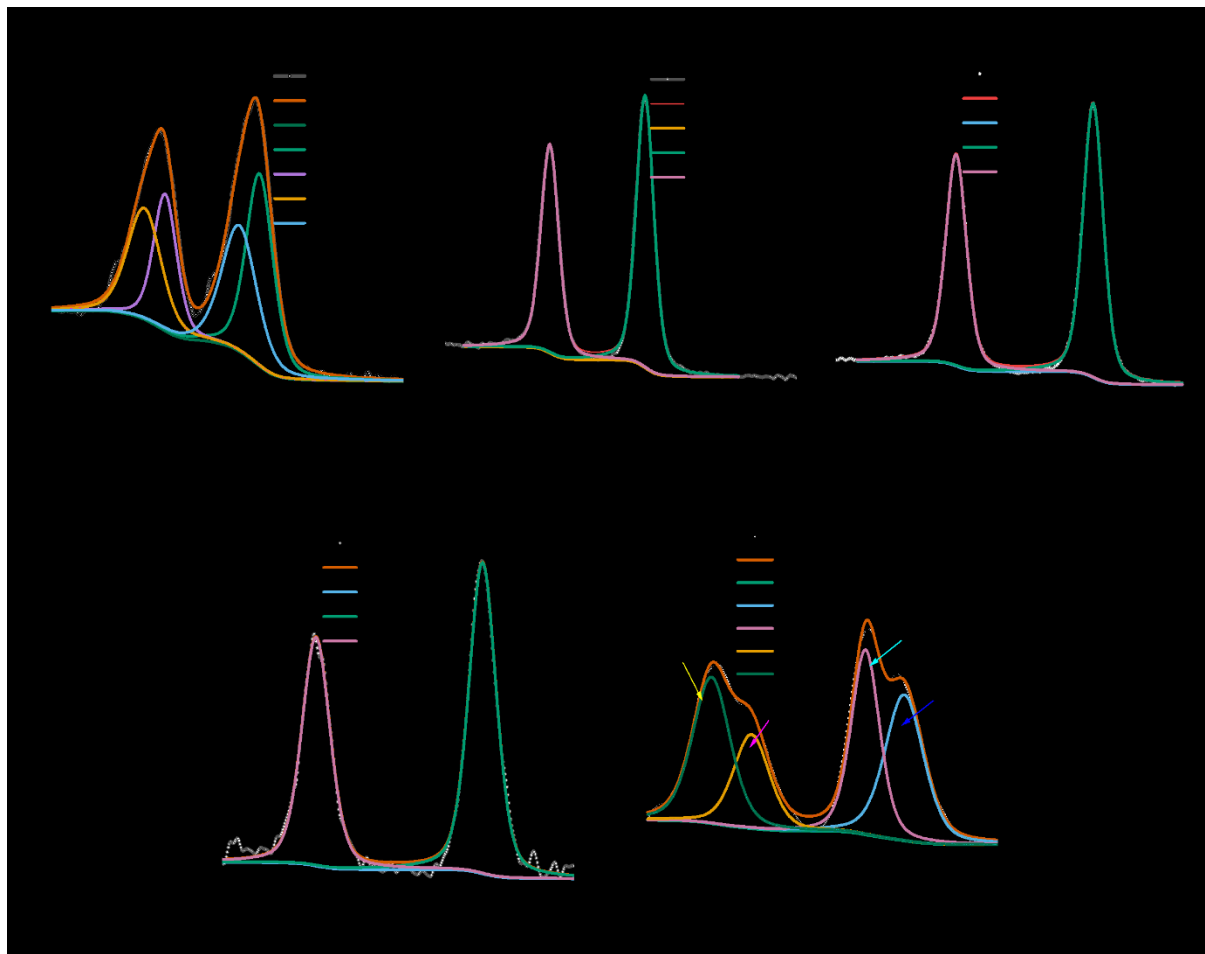


Figure 3. (a), (b), (c), (d), (e) X-ray Photoelectron Spectroscopy spectra of $\text{BA}_2\text{FA}(\text{Pb}_{1-x}\text{Sn}_x)_2\text{I}_7$ deposited at various precursor ratios.

Figure 4a shows the UV-Vis spectra of $\text{BA}_2\text{FA}(\text{Pb}_{1-x}\text{Sn}_x)_2\text{I}_7$ recorded in absorption mode from 400 nm to 800 nm. An absorption spectrum of Sn0 shows a strong absorption peak at 568 nm, which can be attributed to the excitonic transition originating from the $n=2$ phase. A small peak at 617 nm is also observed, which can be assigned to the $n = 3$ phase. The intensity of the peak at 617 nm is less with respect to the peak at 568 nm due to the decreasing exciton binding energy with the n value increasing^{21,28,29,37}. As we partially substitute Pb with Sn, the vital excitonic feature in absorption spectra is diminished, and a low-intensity absorption peak emerges for Sn25 and Sn50 along with redshift. It is observed that as the Sn substitutes Pb, the bandgap of quasi perovskite reduces^{21,28,29,37-41}. Hence, it can be concluded that partial substitution of Pb by Sn can help prepare phase pure Quasi 2D perovskite ($n=2$) with increased absorption spectral region. The room temperature bandgap of Sn0, Sn25 and Sn50

are estimated from the Tauc plot (plot of $(\alpha h\nu)^2$ vs. $h\nu$ where) as shown in Figure 4a and are 2.22 eV, 1.92 eV and 1.71 eV respectively. It is evident from the UV-Vis analysis that as the Sn concentration increases in replacing Pb, there is a noticeable change in bandgap and excitonic character. The wavelength of 473 nm was used to excite the Quasi $\text{BA}_2\text{FA}(\text{Pb}_{1-x}\text{Sn}_x)_2\text{I}_7$ ($x = 0 - 50\%$) samples, and room temperature (RT) PL spectra were recorded in the range from 530 nm to 800 nm as shown in Figure 4b. The RTPL spectra of the Sn0 ($x = 0$) sample show emission peaks at ~ 577 nm and ~ 632 nm, which can be correlated with the absorption spectra with a Stokes shift. The peaks at ~ 577 nm and ~ 632 nm correspond to exciton emission of $n = 2$ and $n = 3$ phases respectively^{21,28,29,37–42}. Unexpectedly, an absorption peak is absent in the 700–800 nm range. This absence implies that the emission peak around 775 nm does not result from exciton emission or bandgap emission^{21,28,29,37–42}. In the case of Sn25 and Sn50 samples, different emission peaks were observed at ~ 575 nm and ~ 705 nm which can be assigned to the exciton emission arising from $\text{BA}_2\text{FAPb}_2\text{I}_7$ and $\text{BA}_2\text{FASn}_2\text{I}_7$ phases respectively^{21,28,29,37–42}. Interestingly, the intensity of exciton emission due to Sn phase at ~ 705 nm is increased as the Sn substitution increased from the Sn25 to the Sn50 sample.

To investigate the carrier recombination processes, we measured the lifetime of samples at RT with a laser excitation wavelength of 405 nm having a pulse width of $<70\text{ps}$ shown in Figure 4c. The experimental data is fitted with the bi-exponentials function:

Where τ_1 fast decay and τ_2 slow decay respectively. The estimated carrier lifetimes at 570 nm for all the samples are shown in Table 1.

Table 1. Lifetime Measurements of Sn0, Sn25, and Sn50.

Sample	Lifetime (ns)
Sn0	$\tau_1 = 0.314, \tau_2 = 3.513$
Sn25	$\tau_1 = 0.481, \tau_2 = 3.009$
Sn50	$\tau_1 = 0.301, \tau_2 = 2.423$

The carrier lifetime associated with fast decay component τ_1 is large in Sn25 thin films, while Sn0 and Sn50 have a low lifetime, indicating fast charge carrier recombination. Previously, various researchers have proved that perovskites with a 50:50 composition of Pb: Sn possess shallow traps, while the perovskites with less Sn exhibit deep trap states. We also found that

the τ_2 for Sn50 is lower than Sn25, corroborating trap-assisted recombination is less in Sn50 than in Sn25. In the case of the Sn50 sample, as Sn is substituting Pb and occupying the Pb vacancies, the trap-assisted carrier lifetime is decreased^{21,28,29}. In 2D perovskite, the dielectric and quantum confinement effects are crucial in shaping their optical and electrical properties. This influence leads to robust excitonic effects and intricate exciton physics, encompassing biexcitons and triexcitons. Consequently, the luminescence of these stratified compounds typically showcases a dominant narrow-band free exciton emission. Interestingly, some systems deviate from the norm and exhibit broadband emission characterized by a substantial Stokes shift. Certain instances even demonstrate photon emission spanning the entire visible spectrum, yielding broad-spectrum white light emission. Self-trapped excitons (STEs) are commonly acknowledged as the primary factor influencing broadband features. In this scenario, charge carriers interact with the soft lattice, inducing elastic structural distortions that lower the system's energy. Due to their transient quasiparticle nature, STEs cannot be directly excited from the ground state by below-gap light. This self-trapping process may be intrinsic, occurring due to transient elastic lattice deformation upon illumination, or extrinsic, where initial local potential wells in a host material serve as nucleating sites for subsequent self-trapping events. Nevertheless, self-trapping is not the sole mechanism responsible for inducing broad photoluminescence. Permanent structural defects and dopants can also induce in-gap states, broadening the emission. In such cases, excitons are presumed to be trapped in an in-gap state, resulting in Stokes-shifted emission. Given the similarities in luminescence characteristics between in-gap states and STEs, their disentanglement has proven challenging^{38,42}. Temperature-dependent photoluminescence (TDPL) measurements were conducted on all samples from 80K to 300K. Figure 4d-f shows the TDPL spectra of Sn0, Sn25, and Sn50, respectively. At low temperatures (80K), the PL spectrum of Sn0(Figure 4d) shows three peaks located at ~578 nm, ~628 nm, and ~670 nm, respectively. The peak at 578 nm is attributed to the excitonic emission of $n = 2$ phase, and the PL at around ~628 nm may be an exciton emission of $n = 3$ phase, which indicates that the mixed phase of $n = 2$ and $n = 3$ phases are present in the thin films. Increasing the temperature from 80 K to 300 K decreases the intensity of peaks. The $n=3$ peak at around ~120K starts to split into two peaks and becomes prominent as the temperature decreases to 77K, which can be assigned to the order-disorder phase change of $n=3$ ^{21,28,38,40-42}. A relatively broad emission band obtained at low temperatures below the band gap energy (~670 nm) can be ascribed to STEs. A large amount of self-trapped excitons (STEs) exists in 2D perovskites owing to the strong electron-lattice or hole-lattice coupling. This effect can significantly promote radiative recombination and

favours light emission. The peak at 670 nm disappears for higher temperatures, which is attributed to the redistribution of charge carriers between the states when localized carriers have sufficient thermal energy to escape and transfer to the dominant transition. When the temperature is increased above 200K, one more peak starts appearing at ~777 nm. With further increase in temperature, the intensity of this peak increases while the intensity of peaks at ~577 nm and ~628 nm decreases. This confirms that the PL peaks at ~577 nm and ~628 nm come from exciton emission, and the peak at around ~777 nm comes from the defect. This radiative defect luminescence may arise from the contribution of vacancies (halide, Pb^{2+} , FA^+) and interstitials (halide, FA^+). According to the previous reports, the luminescence from such defects is usually considered because of shallow defects^{21,28,38,40–42}. In the case of Sn25, as seen in (Figure 4e), three peaks positioned at ~577 nm, ~622 nm, and ~670 nm are observed, just like the Sn0 sample. As the temperature decreases, the intensity of these peaks increases with a very little shift. This shift can be due to the structural phase change of spacer cations. The STE emission at ~670 nm is less intense than the Sn0 sample. The replacement of Pb^{2+} by Sn^{2+} has been contemplated, with Tin (II) being considered the most suitable candidate due to its similar electronic states with lone-pair orbitals. Consequently, the substitution is anticipated to introduce minimal perturbation to the lattice structure. (Figure 4f shows) the TDPL spectra of Sn50 sample shows the presence of two peaks located at around 581 nm and 617 nm. The STE emission is not observed in the case of the Sn50 sample. Compared to Sn0 and Sn25, a red shift is observed in the case of the PL peak of Sn50, which is located at around 581 nm. On the other hand, the peak located at 617 nm blue shifts when compared with Sn0 and Sn25. Also, both peaks are broadened in Sn50 samples.^{21,28,36,38}

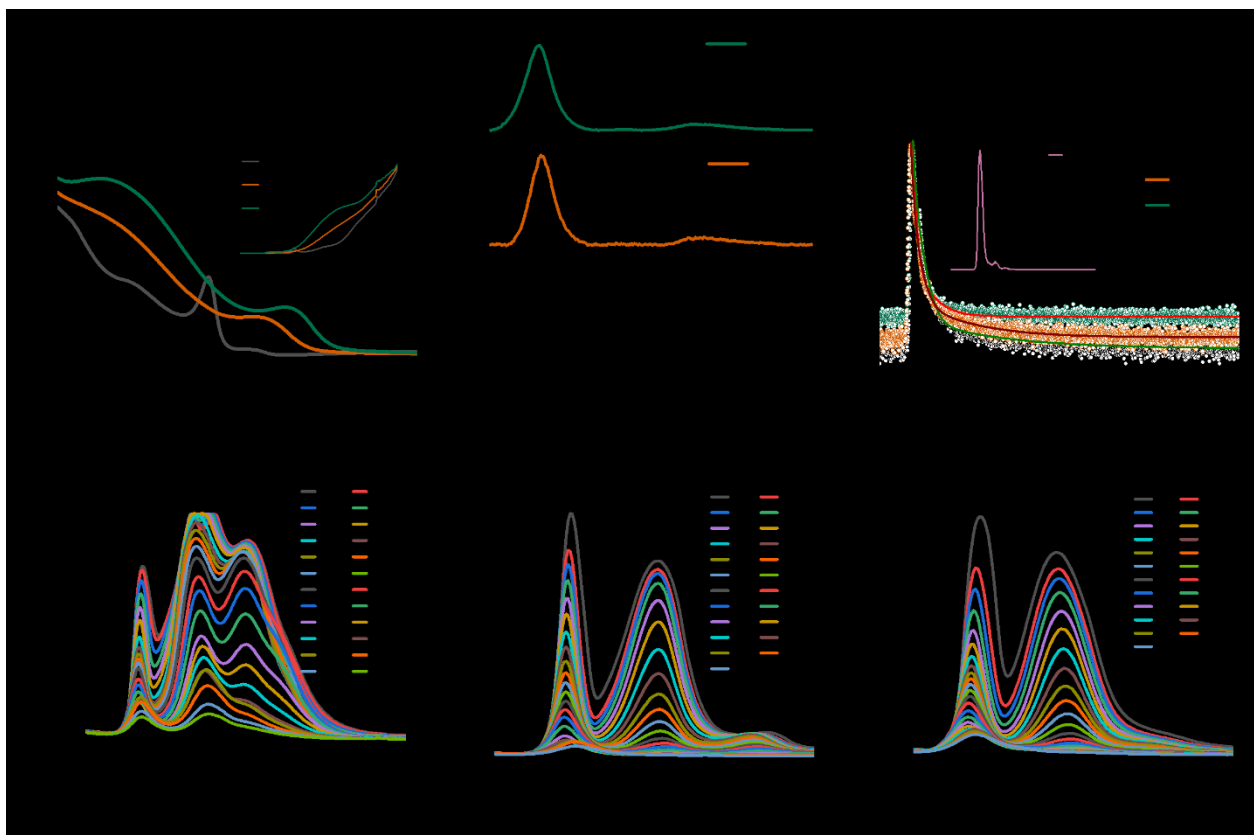


Figure 4. (a) Ultraviolet-visible spectra and Tauc Plot, (b) Room temperature photoluminescence spectra, (c) Time-resolved photoluminescence spectra, (d), (e), (f) Temperature-Dependent Photoluminescence Plots at temperatures range (80K – 300K) deposited of $\text{BA}_2\text{FA}(\text{Pb}_{1-x}\text{Sn}_x)_2\text{I}_7$ deposited at various precursors ratios.

Figure 5a-c shows Density functional theory calculations for Sn0, Sn25, and Sn50 samples in which we find that significant distortion and rotation of the Formamidinium (FA) ion arise upon 25% Sn incorporation. This distortion occurs due to the disparity in ionic radius and chemical properties between lead (Pb) and tin (Sn) ions. The smaller size of Sn^{2+} ions compared to Pb^{2+} ions create lattice strain as they fit into the crystal lattice originally suitable for larger ions, leading to a distortion of the lattice structure. Additionally, introducing Sn ions alters the electrostatic interactions and charge distribution within the lattice, impacting its electronic properties. However, at higher incorporation levels, such distortion is slightly reduced, for example, in 50% Sn concentration, possibly due to more dispersed occupancy of Sn ions, leading to improved homogeneity and reduced local unevenness through a more homogeneous distribution of Sn ions. Sn incorporation causes a significant reduction in the band gap. Increasing the Sn concentration reduces it further, in accordance with the experimental results. The structures show no spin polarisation. Furthermore, the occurrence of a weakly dispersing trap band was found by Sn doping and prominent in the 25% clustered incorporation case shown in Figure 5d-f.

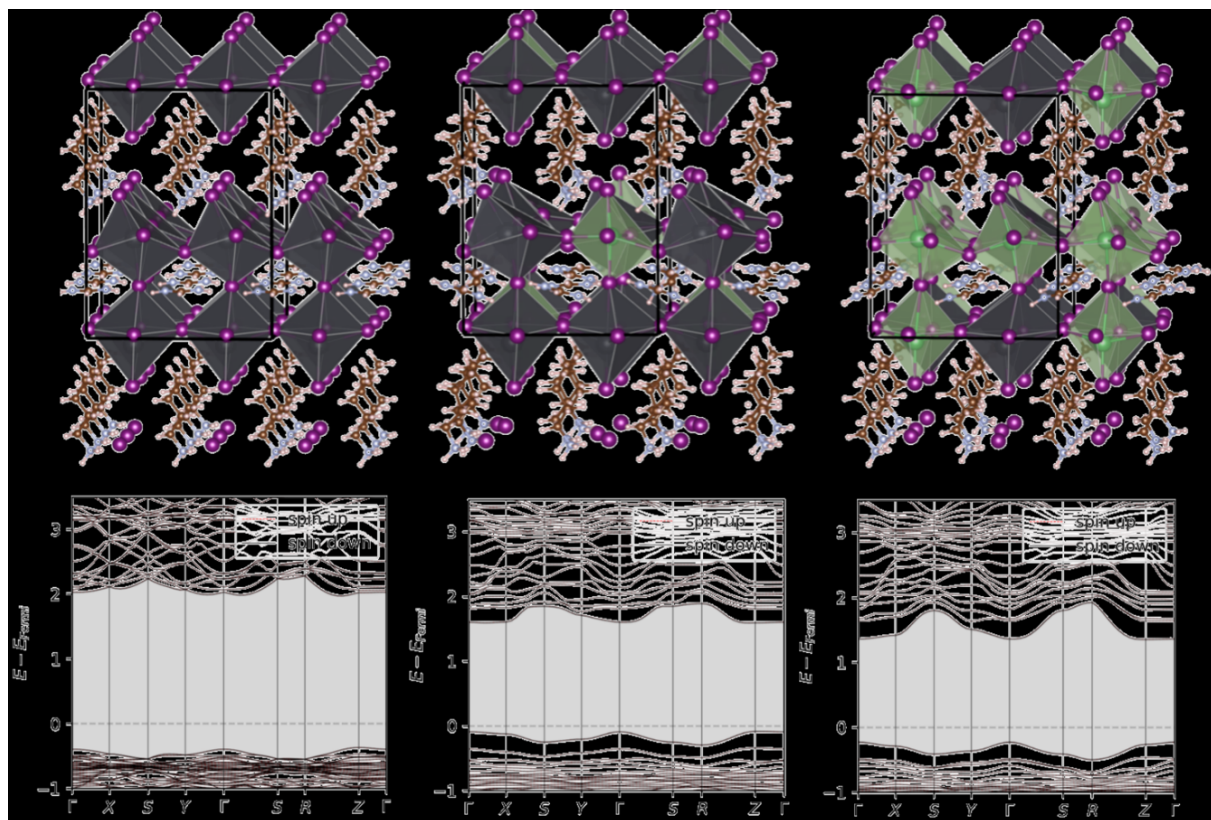


Figure 5. DFT-based crystal structures of (a) $\text{BA}_2\text{FAPb}_2\text{I}_7$ (b) $\text{BA}_2\text{FA}(\text{Pb}_{0.75}\text{Sn}_{0.25})_2\text{I}_7$, (c) $\text{BA}_2\text{FA}(\text{Pb}_{0.5}\text{Sn}_{0.5})_2\text{I}_7$ and (d), (e), (f) shows calculated Band structures (Density of States) using GGA PBE of $\text{BA}_2\text{FA}(\text{Pb}_{1-x}\text{Sn}_x)_2\text{I}_7$ deposited at various precursors ratios.

Figure 6a-c shows notable anodic and cathodic peaks at 1.67 and 0.64 V for Sn0, on the contrary, at 1.4 and 0.58 V for Sn25, also at 1.25 and 0.54 V for Sn50 samples. Anodic and cathodic peaks, observed in the electrochemical processes emerging at the semiconductor electrode interface, directly correspond with removing electrons from the Valence Band (VB) edge and adding electrons to the Conduction Band (CB) edge. Electron affinities and ionization potential can be deduced from these anodic and cathodic peaks. As a result, the electrochemical bandgap estimated from the potential difference between the peaks is 2.31 V, 1.98 V, and 1.79 V for Sn0, Sn25, and Sn50, respectively. These values match closely with the respected optical bandgap estimated from the UV-visible spectrum-based Tauc plot. Table 2 shows the positions of the Valence Band Edge and Conduction Band edge measured from the Normal Hydrogen Electrode (NHE) and local vacuum for Sn0, Sn25, and Sn50, respectively. Figures 6d, e, and f are the scan rate-dependent CV measurements for Sn0, Sn25, and Sn50 respectively. The relationship between peak current and the square root of the scan rate indicates the reversibility of the reaction; a direct proportion suggests reversibility, while deviations imply quasi-reversibility. Furthermore, a linear correlation between peak

current and the square root of the scan rate implies a diffusion-controlled reaction..^{31,32} Figure 6g shows the Band Alignment diagram of TiO₂, Sn0, Sn25, Sn50, and SnO₂ in which CBM, VBM positions, and Band gap values of respective materials are observed. To understand the viability of 2D-Pb-Sn mixed perovskites in devices, the effects of the band offsets of the perovskite layer with TiO₂ and SnO₂ electron transport layer configurations were analyzed in Sn-Pb-based 2D perovskites. We estimated conduction band offsets using valence band minimum (VBM) and conduction band maximum (CBM) to examine the electron transfer phenomena. The results demonstrated that the interface between SnO₂ and 2D perovskites facilitates far more efficient electron transport than TiO₂ owing to their reduced activation barrier for electron transport. This can be explained by the conduction band offset (CBO) between the ETL/perovskite interface and band alignment. The CBO represents the differential in energy between the conduction band minima of the electron transport layer (ETL) and the perovskite layer, denoted as $E_{\text{ETL}} - E_{\text{Perovskite}}$. This metric is pivotal for understanding the electronic compatibility and efficiency of charge transfer between these two materials in optoelectronic applications. The energy level diagram for all three perovskites w.r.t SnO₂ and TiO₂ is shown in Figure 6g. The calculated values of CBO are tabulated in **Table S1**. It is known that if CBO between the ETL/perovskite interface is negative, a cliff forms at the interface that favours electron passage from perovskite to ETL. This observed phenomenon of rapid electron transfer elucidates the preferential selection of SnO₂ as an ETL. The CBO values for perovskites with varying compositions Pb-rich, moderate, and Sn-rich when interfaced with SnO₂ are recorded at -0.4, -0.34, and -0.3 eV, respectively. These findings indicate that Sn-rich perovskites exhibit the highest efficiency as an absorber layer, underscoring the critical role of SnO₂ ETL in providing important guidelines for designing combinations of ETL and perovskite layers.^{43–45} Additionally, the synthesis of TiO₂ and SnO₂ was carried out by spin coating followed by annealing. Figures S5 and S6 show structural and optical characterizations carried out by XRD and FESEM to observe the structural behaviour of TiO₂ and SnO₂^{46,47} and compared with Sn0, Sn25, and Sn50.

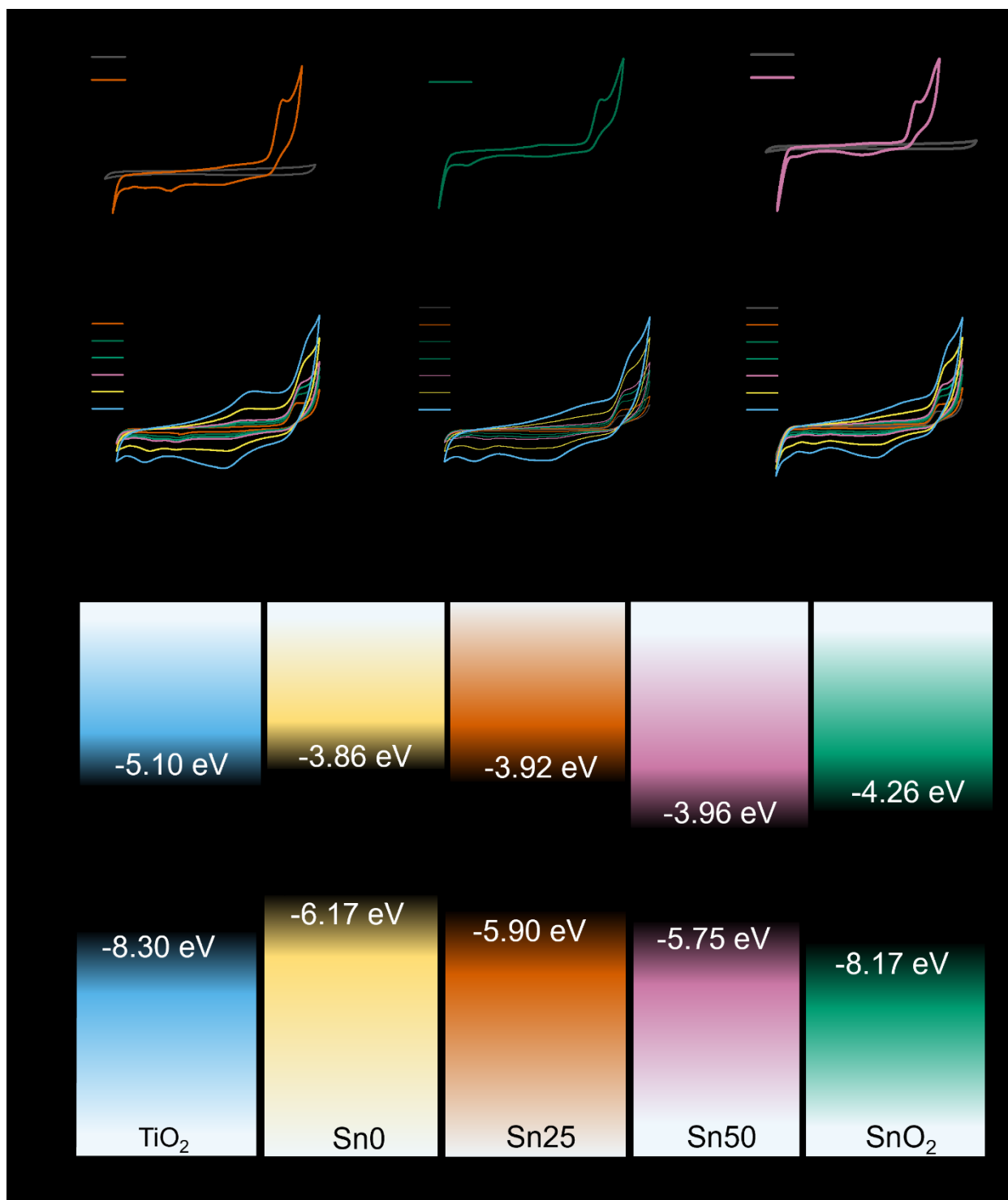


Figure 6. (a), (b) and (c) shows a Cyclic voltammogram for Sn0, Sn25, and Sn50, respectively, recorded on a drop-casted Glassy carbon at a scan rate of 50 mV/s. (The black line is for the blank electrolyte, and the coloured lines are for samples) (d), (e) and (f) show Scan rate dependent ($v = 10$ -500mV) CV responses for the understanding of reaction kinetics in Sn0, Sn25 and Sn50, respectively.

Table 2. Electrochemical band structure parameters (Valence band (VB) and conduction band (CB) edges vs. NHE and vacuum) and the band gap values (E_c = Electrochemical Bandgap and E_g = Optical Bandgap) estimated from the Cyclic Voltammetry V.

Sample	VBM vs NHE(V)	CBM vs NHE(V)	VBM vs Vacuum(eV)	CBM vs Vacuum(eV)	E _c (eV)	E _g (eV)
Sn0	1.67	-0.64	-6.17	-3.86	2.31	2.22
Sn25	1.4	-0.58	-5.9	-3.92	1.98	1.92
Sn50	1.25	-0.54	-5.75	-3.96	1.79	1.71

CONCLUSION

In summary, we have reported mixed Pb-Sn-based 2D Ruddlesden-Popper thin films prepared by a simple solution-based one-step spin coating method followed by annealing. By substituting Pb with Sn, we observed peak broadening and increased microstrain and dislocation density from XRD. It can be concluded that this substitution showed a decrease in bandgap and a change in excitonic character. The presence of mixed-phase, n=2 and n=3 phases were confirmed from excitonic emission at designated positions and a peak at ~777 nm appears due to defects for Pb rich sample. For Sn0 and Sn50 samples, with the decrease in temperature, the intensity of peaks was increased along with redshift. Also, it was confirmed that after the substitution by Sn, STE emission was not as intense as Pb rich Sn0 sample. Time-resolved PL showed that decay was increased for the Sn25 sample due to increased defect states by Pb vacancies. Further, upon Sn substitution, decay was again decreased for Sn50 sample. By cyclic voltammetry, it was confirmed that the obtained electronic bandgap closely resembles the optical bandgap, and a reduction in anodic peaks and an increase in cathodic peaks were observed due to the substitution of Pb with Sn. Further, the DFT calculations confirmed the synergistic of lattice strain due to ionic radius variation (b/w Sn and Pb) and distortions in FA cation on electronic properties of the perovskite.

ACKNOWLEDGMENT

S.S.D. and S.R.R. acknowledge the support of the Department of Materials Engineering, Indian Institute of Science (IISc), Bangalore, India. S.S.D. acknowledges the Indian Institute of Science (IISc), Bangalore, for a fellowship from GATE mode. S.R.R. acknowledges the Science and Engineering Research Board (SERB), Govt. of India for funding (Grant No. EEQ/2022/000697). S.S.D and S.R.R. recognise the support of the Advanced Facility for Microscopy and Microanalysis (AFMM), Centre for Nanoscience and Engineering (CeNSE),

Solid State and Structural Chemistry Unit (SSCU), Indian Institute of Science, Bengaluru, India.

ASSOCIATED CONTENT

Supporting Information

Figure S1: Schematic Diagram of Synthesis Procedure; Figure S2: XRD (2θ Shifting); Figure S3: FESEM images of Sn0, Sn25, Sn50; Figure S4: Survey scan XPS spectra for Sn0, Sn25, Sn50; Figure S5: XRD, FESEM Data of SnO₂; Figure S6: XRD, FESEM Data of TiO₂

AUTHOR INFORMATION

Corresponding Author

Dr. Sachin R. Rondiya

Department of Materials Engineering, Indian Institute of Science, Bangalore 560012, India

Email: rondiya@iisc.ac.in

CONFLICTS OF INTEREST

The authors declare no competing financial interest.

REFERENCES

- (1) Chen, Y.; Sun, Y.; Peng, J.; Tang, J.; Zheng, K.; Liang, Z. 2D Ruddlesden–Popper Perovskites for Optoelectronics. *Advanced Materials* **2018**, *30* (2), 1703487. <https://doi.org/10.1002/adma.201703487>.
- (2) Kim, G.; Petrozza, A. Defect Tolerance and Intolerance in Metal Halide Perovskites. *Advanced Energy Materials* **2020**, *10* (37), 2001959. <https://doi.org/10.1002/aenm.202001959>.
- (3) Zhou, Y.; Poli, I.; Meggiolaro, D.; De Angelis, F.; Petrozza, A. Defect Activity in Metal Halide Perovskites with Wide and Narrow Bandgap. *Nat Rev Mater* **2021**, *6* (11), 986–1002. <https://doi.org/10.1038/s41578-021-00331-x>.
- (4) Cao, X.; Zhi, L.; Jia, Y.; Li, Y.; Zhao, K.; Cui, X.; Ci, L.; Zhuang, D.; Wei, J. A Review of the Role of Solvents in Formation of High-Quality Solution-Processed Perovskite Films. *ACS Appl. Mater. Interfaces* **2019**, *11* (8), 7639–7654. <https://doi.org/10.1021/acsami.8b16315>.

- (5) Ban, M.; Zou, Y.; Rivett, J. P. H.; Yang, Y.; Thomas, T. H.; Tan, Y.; Song, T.; Gao, X.; Credgington, D.; Deschler, F.; Srimringhaus, H.; Sun, B. Solution-Processed Perovskite Light Emitting Diodes with Efficiency Exceeding 15% through Additive-Controlled Nanostructure Tailoring. *Nat Commun* **2018**, *9* (1), 3892. <https://doi.org/10.1038/s41467-018-06425-5>.
- (6) Kuo, M.-Y.; Spitha, N.; Hautzinger, M. P.; Hsieh, P.-L.; Li, J.; Pan, D.; Zhao, Y.; Chen, L.-J.; Huang, M. H.; Jin, S.; Hsu, Y.-J.; Wright, J. C. Distinct Carrier Transport Properties Across Horizontally vs Vertically Oriented Heterostructures of 2D/3D Perovskites. *J. Am. Chem. Soc.* **2021**, *143* (13), 4969–4978. <https://doi.org/10.1021/jacs.0c10000>.
- (7) Yan, L.; Ma, J.; Li, P.; Zang, S.; Han, L.; Zhang, Y.; Song, Y. Charge Carrier Transport in Quasi 2D Ruddlesden–Popper Perovskite Solar Cells. *Advanced Materials* **2022**, *34* (7), 2106822. <https://doi.org/10.1002/adma.202106822>.
- (8) He, T.; Jiang, Y.; Xing, X.; Yuan, M. Structured Perovskite Light Absorbers for Efficient and Stable Photovoltaics. *Advanced Materials* **2020**, *32* (26), 1903937. <https://doi.org/10.1002/adma.201903937>.
- (9) Kazim, S.; Nazeeruddin, M. K.; Grätzel, M.; Ahmad, S. Perovskite as Light Harvester: A Game Changer in Photovoltaics. *Angew Chem Int Ed* **2014**, *53* (11), 2812–2824. <https://doi.org/10.1002/anie.201308719>.
- (10) Ma, C.; Leng, C.; Ji, Y.; Wei, X.; Sun, K.; Tang, L.; Yang, J.; Luo, W.; Li, C.; Deng, Y.; Feng, S.; Shen, J.; Lu, S.; Du, C.; Shi, H. 2D/3D Perovskite Hybrids as Moisture-Tolerant and Efficient Light Absorbers for Solar Cells. *Nanoscale* **2016**, *8* (43), 18309–18314. <https://doi.org/10.1039/C6NR04741F>.
- (11) Li, P.; Zhang, Y.; Liang, C.; Xing, G.; Liu, X.; Li, F.; Liu, X.; Hu, X.; Shao, G.; Song, Y. Phase Pure 2D Perovskite for High Performance 2D–3D Heterostructured Perovskite Solar Cells. *Advanced Materials* **2018**, *30* (52), 1805323. <https://doi.org/10.1002/adma.201805323>.
- (12) Xiao, X.; Wu, M.; Ni, Z.; Xu, S.; Chen, S.; Hu, J.; Rudd, P. N.; You, W.; Huang, J. Ultrafast Exciton Transport with a Long Diffusion Length in Layered Perovskites with Organic Cation Functionalization. *Advanced Materials* **2020**, *32* (46), 2004080. <https://doi.org/10.1002/adma.202004080>.
- (13) Chen, Y.; Yi, H. T.; Wu, X.; Haroldson, R.; Gartstein, Y. N.; Rodionov, Y. I.; Tikhonov, K. S.; Zakhidov, A.; Zhu, X.-Y.; Podzorov, V. Extended Carrier Lifetimes and Diffusion

- in Hybrid Perovskites Revealed by Hall Effect and Photoconductivity Measurements. *Nat Commun* **2016**, *7* (1), 12253. <https://doi.org/10.1038/ncomms12253>.
- (14) Wu, G.; Liang, R.; Zhang, Z.; Ge, M.; Xing, G.; Sun, G. 2D Hybrid Halide Perovskites: Structure, Properties, and Applications in Solar Cells. *Small* **2021**, *17* (43), 2103514. <https://doi.org/10.1002/sml.202103514>.
- (15) Mauck, C. M.; Tisdale, W. A. Excitons in 2D Organic–Inorganic Halide Perovskites. *Trends in Chemistry* **2019**, *1* (4), 380–393. <https://doi.org/10.1016/j.trechm.2019.04.003>.
- (16) Deng, S.; Shi, E.; Yuan, L.; Jin, L.; Dou, L.; Huang, L. Long-Range Exciton Transport and Slow Annihilation in Two-Dimensional Hybrid Perovskites. *Nat Commun* **2020**, *11* (1), 664. <https://doi.org/10.1038/s41467-020-14403-z>.
- (17) Katan, C.; Mercier, N.; Even, J. Quantum and Dielectric Confinement Effects in Lower-Dimensional Hybrid Perovskite Semiconductors. *Chem. Rev.* **2019**, *119* (5), 3140–3192. <https://doi.org/10.1021/acs.chemrev.8b00417>.
- (18) Hu, J.; Yan, L.; You, W. Two Dimensional Organic–Inorganic Hybrid Perovskites: A New Platform for Optoelectronic Applications. *Advanced Materials* **2018**, *30* (48), 1802041. <https://doi.org/10.1002/adma.201802041>.
- (19) Li, X.; Hoffman, J. M.; Kanatzidis, M. G. The 2D Halide Perovskite Rulebook: How the Spacer Influences Everything from the Structure to Optoelectronic Device Efficiency. *Chem. Rev.* **2021**, *121* (4), 2230–2291. <https://doi.org/10.1021/acs.chemrev.0c01006>.
- (20) Fu, P.; Quintero, M. A.; Vasileiadou, E. S.; Raval, P.; Welton, C.; Kepenekian, M.; Volonakis, G.; Even, J.; Liu, Y.; Malliakas, C.; Yang, Y.; Laing, C.; Dravid, V. P.; Reddy, G. N. M.; Li, C.; Sargent, E. H.; Kanatzidis, M. G. Chemical Behavior and Local Structure of the Ruddlesden–Popper and Dion–Jacobson Alloyed Pb/Sn Bromide 2D Perovskites. *J. Am. Chem. Soc.* **2023**, *145* (29), 15997–16014. <https://doi.org/10.1021/jacs.3c03997>.
- (21) Fang, H.; Tekelenburg, E. K.; Xue, H.; Kahmann, S.; Chen, L.; Adjokatse, S.; Brocks, G.; Tao, S.; Loi, M. A. Unraveling the Broadband Emission in Mixed Tin Lead Layered Perovskites. *Advanced Optical Materials* **2023**, *11* (4), 2202038. <https://doi.org/10.1002/adom.202202038>.
- (22) Wang, Z.; Wang, F.; Zhao, B.; Qu, S.; Hayat, T.; Alsaedi, A.; Sui, L.; Yuan, K.; Zhang, J.; Wei, Z.; Tan, Z. Efficient Two-Dimensional Tin Halide Perovskite Light-Emitting Diodes via a Spacer Cation Substitution Strategy. *J. Phys. Chem. Lett.* **2020**, *11* (3), 1120–1127. <https://doi.org/10.1021/acs.jpcllett.9b03565>.

- (23) Kojima, A.; Teshima, K.; Shirai, Y.; Miyasaka, T. Organometal Halide Perovskites as Visible-Light Sensitizers for Photovoltaic Cells. *J. Am. Chem. Soc.* **2009**, *131* (17), 6050–6051. <https://doi.org/10.1021/ja809598r>.
- (24) NREL National Renewable Energy Laboratory. *Best Research-Cell Efficiencies Chart-NREL*; 2023. <https://www.nrel.gov/pv/cell-efficiency.html>.
- (25) Lee, H.; Kang, S. B.; Lee, S.; Zhu, K.; Kim, D. H. Progress and Outlook of Sn–Pb Mixed Perovskite Solar Cells. *Nano Convergence* **2023**, *10* (1), 27. <https://doi.org/10.1186/s40580-023-00371-9>.
- (26) Ogomi, Y.; Morita, A.; Tsukamoto, S.; Saitho, T.; Fujikawa, N.; Shen, Q.; Toyoda, T.; Yoshino, K.; Pandey, S. S.; Ma, T.; Hayase, S. $\text{CH}_3\text{NH}_3\text{Sn}_x\text{Pb}_{(1-x)}\text{I}_3$ Perovskite Solar Cells Covering up to 1060 Nm. *J. Phys. Chem. Lett.* **2014**, *5* (6), 1004–1011. <https://doi.org/10.1021/jz5002117>.
- (27) Tong, J.; Jiang, Q.; Ferguson, A. J.; Palmstrom, A. F.; Wang, X.; Hao, J.; Dunfield, S. P.; Louks, A. E.; Harvey, S. P.; Li, C.; Lu, H.; France, R. M.; Johnson, S. A.; Zhang, F.; Yang, M.; Geisz, J. F.; McGehee, M. D.; Beard, M. C.; Yan, Y.; Kuciauskas, D.; Berry, J. J.; Zhu, K. Carrier Control in Sn–Pb Perovskites via 2D Cation Engineering for All-Perovskite Tandem Solar Cells with Improved Efficiency and Stability. *Nat Energy* **2022**, *7* (7), 642–651. <https://doi.org/10.1038/s41560-022-01046-1>.
- (28) Xian, S.; Hou, S.; Zhang, H.; Yang, J.; Pan, G.; Gao, H.; You, W.; Zhang, Z.; Zhu, B.; Mao, Y. High Quality Quasi-Two-Dimensional Organic–Inorganic Hybrid Halide Perovskite Film for High Performance Photodetector. *Applied Physics Letters* **2023**, *122* (10), 103503. <https://doi.org/10.1063/5.0139686>.
- (29) Yang, Y.; Zhang, H.; Hou, S.; Wang, T.; Chen, W.; Xian, S.; Zhang, Z.; Mao, Y. Sn-Based Quasi-Two-Dimensional Organic–Inorganic Hybrid Halide Perovskite for High-Performance Photodetectors. *Applied Physics Letters* **2021**, *119* (16), 161106. <https://doi.org/10.1063/5.0068273>.
- (30) Narra, S.; Lin, C.-Y.; Seetharaman, A.; Jokar, E.; Diau, E. W.-G. Femtosecond Exciton and Carrier Relaxation Dynamics of Two-Dimensional (2D) and Quasi-2D Tin Perovskites. *J. Phys. Chem. Lett.* **2021**, *12* (51), 12292–12299. <https://doi.org/10.1021/acs.jpcclett.1c03427>.
- (31) Wadhai, S.; Jadhav, Y.; Thakur, P. Synthesis of Metal-Free Phosphorus Doped Graphitic Carbon Nitride-P25 (TiO₂) Composite: Characterization, Cyclic Voltammetry and Photocatalytic Hydrogen Evolution. *Solar Energy Materials and Solar Cells* **2021**, *223*, 110958. <https://doi.org/10.1016/j.solmat.2021.110958>.

- (32) Rondiya, S. R.; Buldu, D. G.; Brammertz, G.; Jadhav, Y. A.; Cross, R. W.; Ghosh, H. N.; Davies, T. E.; Jadkar, S. R.; Dzade, N. Y.; Vermang, B. Revealing the Electronic Structure, Heterojunction Band Offset and Alignment of $\text{Cu}_2\text{ZnGeSe}_4$: A Combined Experimental and Computational Study towards Photovoltaic Applications. *Phys. Chem. Chem. Phys.* **2021**, 23 (15), 9553–9560. <https://doi.org/10.1039/D0CP06143C>.
- (33) Jadhav, Y. A.; Thakur, P. R.; Haram, S. K. Voltammetry Investigation on Copper Zinc Tin Sulphide /Selenide (CZTSxSe_{1-x}) Alloy Nanocrystals: Estimation of Composition Dependent Band Edge Parameters. *Solar Energy Materials and Solar Cells* **2016**, 155, 273–279. <https://doi.org/10.1016/j.solmat.2016.06.030>.
- (34) Inamdar, S. N.; Ingole, P. P.; Haram, S. K. Determination of Band Structure Parameters and the Quasi Particle Gap of CdSe Quantum Dots by Cyclic Voltammetry. *ChemPhysChem* **2008**, 9 (17), 2574–2579. <https://doi.org/10.1002/cphc.200800482>.
- (35) Saykar, N. G.; Iqbal, M.; Pawar, M.; Chavan, K. T.; Mahapatra, S. K. Dual-Functional 3-Acetyl-2,5-Dimethylthiophene Additive-Assisted Crystallization Control and Trap State Passivation for High-Performance Perovskite Solar Cells. *ACS Appl. Energy Mater.* **2022**, 5 (12), 14701–14711. <https://doi.org/10.1021/acsaem.2c01881>.
- (36) Saykar, N. G.; Iqbal, M.; Ray, A. K.; Mahapatra, S. K. Synergistic Effect of Crystallization Control and Defect Passivation Induced by a Multifunctional Primidone Additive for High-Performance Perovskite Solar Cells. *Energy Fuels* **2023**, 37 (1), 675–683. <https://doi.org/10.1021/acs.energyfuels.2c03191>.
- (37) Kamminga, M. E.; Fang, H.-H.; Filip, M. R.; Giustino, F.; Baas, J.; Blake, G. R.; Loi, M. A.; Palstra, T. T. M. Confinement Effects in Low-Dimensional Lead Iodide Perovskite Hybrids. *Chem. Mater.* **2016**, 28 (13), 4554–4562. <https://doi.org/10.1021/acs.chemmater.6b00809>.
- (38) Paritmongkol, W.; Powers, E. R.; Dahod, N. S.; Tisdale, W. A. Two Origins of Broadband Emission in Multilayered 2D Lead Iodide Perovskites. *J. Phys. Chem. Lett.* **2020**, 11 (20), 8565–8572. <https://doi.org/10.1021/acs.jpcllett.0c02214>.
- (39) He, M.; Xu, Z.; Zhao, C.; Gao, Y.; Ke, K.; Liu, N.; Yao, X.; Kang, F.; Shen, Y.; Lin, L.; Wei, G. Sn Based Self Powered Ultrafast Perovskite Photodetectors with Highly Crystalline Order for Flexible Imaging Applications. *Adv Funct Materials* **2023**, 33 (24), 2300282. <https://doi.org/10.1002/adfm.202300282>.
- (40) Lin, C.-W.; Liu, F.; Chen, T.-Y.; Lee, K.-H.; Chang, C.-K.; He, Y.; Leung, T. L.; Ng, A. M. C.; Hsu, C.-H.; Popović, J.; Djurišić, A.; Ahn, H. Structure-Dependent Photoluminescence in Low-Dimensional Ethylammonium, Propylammonium, and

- Butylammonium Lead Iodide Perovskites. *ACS Appl. Mater. Interfaces* **2020**, *12* (4), 5008–5016. <https://doi.org/10.1021/acsami.9b17881>.
- (41) Wu, X.; Trinh, M. T.; Niesner, D.; Zhu, H.; Norman, Z.; Owen, J. S.; Yaffe, O.; Kudisch, B. J.; Zhu, X.-Y. Trap States in Lead Iodide Perovskites. *J. Am. Chem. Soc.* **2015**, *137* (5), 2089–2096. <https://doi.org/10.1021/ja512833n>.
- (42) Kahmann, S.; Tekelenburg, E. K.; Duim, H.; Kamminga, M. E.; Loi, M. A. Extrinsic Nature of the Broad Photoluminescence in Lead Iodide-Based Ruddlesden–Popper Perovskites. *Nat Commun* **2020**, *11* (1), 2344. <https://doi.org/10.1038/s41467-020-15970-x>.
- (43) Lu, X. Room-Temperature Synthesis of Colloidal SnO₂ Quantum Dot Solution and Ex-Situ Deposition on Carbon Nanotubes as Anode Materials for Lithium Ion Batteries. *Journal of Alloys and Compounds* **2016**.
- (44) Park, S. Y.; Zhu, K. Advances in SnO₂ for Efficient and Stable n–i–p Perovskite Solar Cells. *Adv. Mater.* **2022**.
- (45) Yang, D. High Efficiency Planar-Type Perovskite Solar Cells with Negligible Hysteresis Using EDTA-Complexed SnO₂. *NATURE COMMUNICATIONS* **2018**.
- (46) Lin, L.; Jones, T. W.; Wang, J. T.; Cook, A.; Pham, N. D.; Duffy, N. W.; Mihaylov, B.; Grigore, M.; Anderson, K. F.; Duck, B. C.; Wang, H.; Pu, J.; Li, J.; Chi, B.; Wilson, G. J. Strategically Constructed Bilayer Tin (IV) Oxide as Electron Transport Layer Boosts Performance and Reduces Hysteresis in Perovskite Solar Cells. *Small* **2020**, *16* (12), 1901466. <https://doi.org/10.1002/sml.201901466>.
- (47) Scanlon, D. O.; Dunnill, C. W.; Buckeridge, J.; Shevlin, S. A.; Logsdail, A. J.; Woodley, S. M.; Catlow, C. R. A.; Powell, Michael. J.; Palgrave, R. G.; Parkin, I. P.; Watson, G. W.; Keal, T. W.; Sherwood, P.; Walsh, A.; Sokol, A. A. Band Alignment of Rutile and Anatase TiO₂. *Nature Mater* **2013**, *12* (9), 798–801. <https://doi.org/10.1038/nmat3697>.